

# 3D microstructure characterization of polymer battery electrodes by statistical image analysis based on synchrotron X-ray tomography

Matthias Neumann<sup>a,1,\*</sup>, Marten Ademmer<sup>a,1</sup>, Markus Osenberg<sup>b</sup>, André Hilger<sup>b</sup>, Fabian Wilde<sup>c</sup>, Simon Muench<sup>d,e</sup>, Martin D. Hager<sup>d,e</sup>, Ulrich S. Schubert<sup>d,e</sup>, Ingo Manke<sup>b</sup>, Volker Schmidt<sup>a</sup>

<sup>a</sup>*Institute of Stochastics, Ulm University, 89069 Ulm, Germany*

<sup>b</sup>*Institute of Applied Materials, Helmholtz Center for Materials and Energy, 14109 Berlin, Germany*

<sup>c</sup>*Institute of Materials Physics, Helmholtz Center Hereon, 21502 Geesthacht, Germany*

<sup>d</sup>*Laboratory of Organic and Macromolecular Chemistry (IOMC), Friedrich-Schiller University Jena, 07743 Jena, Germany*

<sup>e</sup>*Center for Energy and Environmental Chemistry Jena (CEEC Jena), Friedrich Schiller University Jena, 07743 Jena, Germany*

---

## Abstract

Polymer-based batteries represent a promising concept for next-generation energy storage due to their potentially higher power densities and smaller ecological footprint, compared to classical Li-ion batteries. Since the microstructure of electrodes is a key factor for the performance of battery cells, a detailed understanding of this microstructure is essential for the improvement of manufacturing processes. In the present contribution, the 3D microstructure of electrodes for polymer-based batteries is quantitatively characterized for the first time, where synchrotron X-ray tomography is combined with statistical image analysis. In particular, 3D imaging is performed for two porous electrodes, which both consist of the redox-active polymer PTMA as well as conductive additives, but differ regarding their binder materials. The focus is put on local heterogeneity of volume fractions of the constituents, surface area per unit volume of the polymer phase and the length of shortest transportation paths through both, polymer and binder-additive phase. It is shown that using different binder materials leads to significant differences regarding the 3D electrode microstructures. In this way, statistical analysis of image data helps to gain further insight into the influence of manufacturing processes on electrode microstructures and thus, on the performance of battery cells.

*Keywords:* 3D microstructure characterization, image analysis, polymer battery, PTMA electrode, spatial statistics, synchrotron X-ray tomography.

---

## 1. Introduction

Technological advances, *e.g.*, of consumer electronics and electric vehicles, continuously increase the requirements batteries have to fulfil. This led to the development of many different cell chemistries, optimized for specific applications. For next-generation batteries, one approach consists in using organic polymers as active material of the electrodes. In particular, the electrodes of polymer-based batteries are comprised of polymeric redox-active materials. These batteries gained much interest in recent years, since critical inorganic raw materials (with, *e.g.*, high toxicity, negative environmental impact, and limited availability) can potentially be replaced by readily available polymeric active materials [1]. As circular economy plays an increasingly important role, organic active materials might perspectivevely enable a closed

---

\*Corresponding author. Email: matthias.neumann@uni-ulm.de. Phone: +49 731 50 - 23506. Fax: +49 731 50 - 23649.

<sup>1</sup>MN and MA contributed equally to this paper.

life cycle by the utilization of bio-based organic molecules/polymers [2]. Note that a large variety of different polymeric materials has been studied as cathode and anode materials, respectively [3]. Organic radical batteries (ORBs), which are based on stable radicals, such as the 2,2,6,6-tetramethylpiperidinyl-*N*-oxyl (TEMPO) radical as redox active moieties, have been established two decades ago [4]. Nowadays, the first studied TEMPO-containing polymer poly(2,2,6,6-tetramethyl-4-piperinidyl-*N*-oxyl methacrylate) [5], abbreviated by PTMA, can still be considered as the benchmark material. Electrodes based on this material feature very high power densities, allowing charging within minutes and even seconds [6]. In contrast to conjugated polymers, PTMA-based electrodes require the addition of conductive additives (*i.e.*, various carbon materials) in order to achieve sufficient electronic conductivity [1]. Consequently, the typical composition of such polymer-based electrodes is as follows: ca. 40 to 60 wt% of PTMA, 35 to 55 wt% of the conductive carbon material as well as 2 to 10 wt% binder. As the latter, various polymers have been utilized ranging from standard binder polyvinylidene fluoride (PVDF) via water-soluble carboxymethylcellulose (CMC) to ionic polymers [3]. These complex mixtures will result in different morphologies of the electrode microstructure. It is well-known that the 3D microstructure strongly influences macroscopic physical properties [7, 8] like, *e.g.*, electric conductivity or the access of electrolyte within the electrode. Although these properties depending on the microstructure are, in turn, crucial for the battery’s performance, there are only a few reports in the literature, which deal with the 3D microstructure of polymer-based batteries. So far, the morphology of PTMA-based electrodes has been inspected only qualitatively by means of 2D image data obtained by scanning electron microscopy (SEM), see, *e.g.*, [9] where such electrodes with carbon fibers as conductive additive have been studied.

In the present contribution, synchrotron X-ray tomography, a powerful tool to resolve the microstructure of battery materials [10, 11, 12], is used to acquire 3D image data of PTMA-based electrodes for the first time. Doing so, for two PTMA-based electrodes differing from each other regarding the utilized binder material, the full thickness of the electrodes for an area of  $1\text{ mm} \times 4\text{ mm}$  in lateral direction has been reconstructed at a resolution of  $1\text{ }\mu\text{m}$ . After pre-processing of this 3D image data, tools of spatial statistics and mathematical morphology [13, 14] are used for microstructure characterization. In particular, microstructure descriptors become accessible which can neither be determined experimentally nor on the basis of 2D image data, such as, *e.g.*, shortest-path lengths through a given material phase being important for the quality of charge transport [15, 16]. Note however that this workflow for 3D microstructure characterization, *i.e.*, X-ray tomography, image pre-processing followed by statistical image analysis has already been applied for a variety of differently manufactured metal-based electrodes, see, *e.g.*, [17, 18, 19, 20]. Furthermore, X-ray tomography has also been used to characterize the microstructure of electrodes based on lithium-cobalt oxides ( $\text{LiCoO}_2$ ) and lithium-iron phosphate ( $\text{LiFePO}_4$ ), see, *e.g.*, [21] and [22], respectively. We now transfer the combination of X-ray tomography with statistical image analysis to PTMA-based electrodes, where we put a particular emphasis on local heterogeneities of the analyzed microstructures. This is a first step towards a systematic data-driven microstructure optimization of materials used for polymer-based batteries.

The rest of the present paper is organized as follows. The preparation of the polymer-based cathodes under consideration as well as 3D imaging is described in Section 2. Pre-processing and segmentation of image data is presented in Section 2.4, which provides the basis for the microstructure characterization by means of statistical image analysis in Section 3. Section 4 concludes.

## 2. Materials and Methods

### 2.1. Description of polymer-based cathode materials

Two different polymer electrodes were prepared, denoted as Sample A and Sample B in the following. Both electrodes contain cross-linked PTMA as active material, SuperP<sup>®</sup> as conductive additive, and differ with respect to their binder materials. For Sample A, poly(vinylidene fluoride) (PVdF) was utilized as binder and *N*-methyl pyrrolidone (NMP) was used as solvent for the electrode preparation, resulting in a ratio of PTMA/SuperP<sup>®</sup>/PVdF 60/35/5 (wt/wt/wt). The mixture was dispersed in a lab dissolver and NMP was added until a homogeneous viscous paste was formed. Subsequently, the paste was doctor bladed on an aluminum current collector and dried overnight at 80 °C. For Sample B, carboxymethyl cellulose (CMC) was utilized as binder and water was used as solvent for the electrode preparation, resulting in a ratio of PTMA/SuperP<sup>®</sup>/CMC 60/35/5 (wt/wt/wt). The PTMA was prepared as described in [23]. The mixture was stirred, swollen in water for one day, dispersed in a lab dissolver, and water was added until a homogeneous viscous paste was formed. The aluminum foil was treated with an aqueous potassium hydroxide (KOH) solution (5 wt%) for 1 min and rinsed with distilled water. Subsequently, the paste was doctor bladed on the aluminum foil and dried overnight at 80 °C. Due to the different solvents and binders in both slurries, different amounts of solvent are required to achieve the same viscosity. Thus, the content of solids in both slurries may vary, which results in different mass loadings for similar wet film thicknesses in the doctor blading and, consequently, varying film thicknesses of the dried electrodes.

### 2.2. 3D imaging by synchrotron X-ray tomography

In this section, 3D imaging of the considered cathode materials is described. First, the samples are prepared for synchrotron X-ray tomography, where pieces of the two different cathode materials are cut from the center of each sample (Samples A and B), the size of which is 1 mm × 4 mm in lateral direction (parallel to the aluminum foil) and contain the full thickness of the electrode (orthogonal to the aluminum foil). Due to the application of force on the sample during the cutting process, stress induced deformations of the sample are possible. To account for these deformations that are visible in Figure 1, only the central and less deformed parts of image data are used for statistical analysis (see flat cross section in Figure 3). Furthermore, to assure a stable tomographic scan, both sample pieces are placed in individual stacks between two supporting Plexiglas<sup>®</sup> rods. In addition, to improve stability, the rod preparation also prevents the samples from getting into contact with glue or any other fluid, thereby avoiding a capillary driven filling of the samples. This allows for re-preparations of the electrodes, which – in turn – enables us to perform additional imaging by SEM, see Section 2.3. Since the latter provides image data with a higher resolution, we obtain additional information supporting the segmentation of synchrotron data in Section 2.4.

Sample A has been measured at the Petra III DESY synchrotron facility (Hamburg, Germany) at the P05 beamline [24, 25], operated by Helmholtz-Zentrum Hereon, using an X-ray energy of 15 keV. The transmission through the polymer sample is transformed into visible light by a CdWO<sub>4</sub> scintillator, magnified by a 10× optic and detected with a Ximea CB500MG camera. The whole setup yields a pixel size of 0.46 μm and a resolution of approximately 1.0 μm. Each of the 3001 radiograms is exposed for 0.3 seconds. In addition, 210 flat fields and 20 dark fields are captured. The reconstruction was performed on site using the P05 in-house MATLAB reconstruction software based on filtered back projection [26, 27].

Sample B has been measured similarly, at the BESSY II synchrotron facility (Berlin, Germany) [28] at the BAMline with an X-ray energy of 16 keV. At BAMline, the sample transmission is also transformed by a CdWO<sub>4</sub> scintillator and magnified by a 10× optic but, in contrast to Sample A, detected with a

PCO4000 camera. This setup yields a pixel size of  $0.44\ \mu\text{m}$  and a resolution of approximately  $0.9\ \mu\text{m}$ . Each of the 2256 radiograms is exposed for 1.5 seconds and similarly to Sample A, 170 flat fields and 6 position references are captured. The reconstruction was performed live on site using the BAMline in-house python reconstruction software based on filtered back projection [29].

In both cases, *i.e.*, for the image data of Sample A and Sample B, a varying center of rotation position measurement protocol is used, which allows for a significant reduction of the appearance of ring artifacts. In addition, image data is further processed to remove noise by means of a total variation minimization [30] and the so-called non-local means denoising [31].

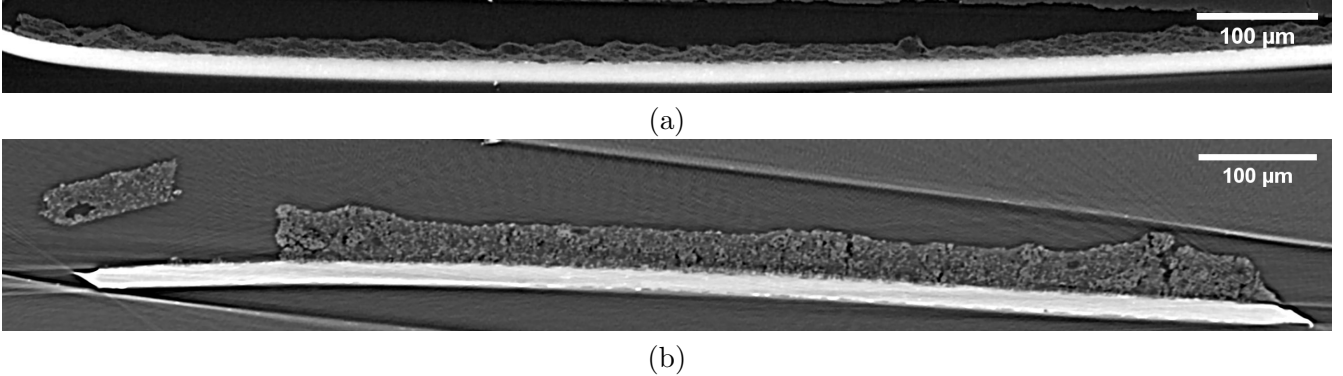


Figure 1: 2D slices of grayscale images representing Sample A (top) and Sample B (bottom). On the left-hand side of Sample B, a part of the electrode has detached from the aluminum foil.

### 2.3. Imaging by scanning electron microscopy

For a guidance of image segmentation and a better understanding of the electrode structure on the sub-micrometer-scale, a cross section with a resolution on the nanometer scale is required. The cross section shown in Figure 2 was measured at Correlative Microscopy and Spectroscopy (CCMS) at Helmholtz-Zentrum Berlin (HZB). A ZEISS Crossbeam 340 was used. For the measurement, the sample previously measured with synchrotron radiation is re-prepared. After disassembling the Plexiglas<sup>®</sup> rod sample holder, the sample is glued with the aluminum foil facing down on a scanning electron microscopy (SEM) pin holder. To prepare the cross section, a part of the sample is removed by means of gallium ion milling. The cross section is then scanned with an electron beam and imaged with an angled chamber SE2-detector.

### 2.4. Image pre-processing and segmentation

In order to characterize the electrode microstructures by means of statistical image analysis, a phase-based segmentation of the grayscale images obtained by synchrotron X-ray microtomography has to be performed. This means that each voxel in the grayscale images, which are visualized in Figure 1, is classified as aluminum foil, polymer, binder-additive phase or micropores. Note that the binder-additive phase contains nanopores, visible in Figure 2, which can not be resolved by synchrotron X-ray microtomography. Prior to segmentation, three steps of image pre-processing are performed. First, that part of Sample B, where the electrode material has detached from the foil (see Figure 1), is removed. Second, a binary mask of both samples is created. For this purpose, a global threshold is used which separates the cathode from the aluminum foil and the background. The mask determined by global thresholding still contains some holes, which are filled by morphological closing [32]. Third, based on the determined mask, the samples are rotated such that they are aligned with the coordinate system. From a technical point of view, the

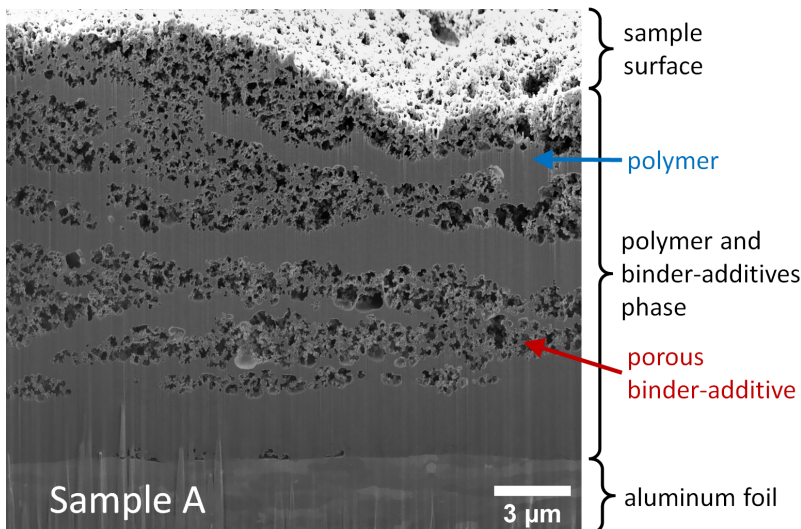


Figure 2: Cross section of Sample A obtained by SEM showing the different phases of the layered electrode structure, i.e. polymer, porous binder-additive and the aluminium foil, at a higher resolution compared to image data obtained by synchrotron X-ray tomography

latter facilitates the microstructure characterization by statistical image analysis performed in Section 3.

After these pre-processing steps, the grayscale images are segmented. In the cross sections presented in Figures 3a and 3c, a binary absorption distribution with bright and dark regions can be observed in combination with mesopores pores and cracks. Considering the SEM cross section, it is clear that the higher absorbing areas represent the polymer phase while the darker and thus less absorbing areas have to represent the porous binder-additive. It turned out that global thresholding is appropriate for Sample A, *i.e.*, each voxel is classified according to globally defined ranges of grayscale values attributed to the different phases. These ranges, given in Table 1, are manually chosen.

phase	micropores	binder-additive phase	polymer	aluminum foil
Sample A	1 – 21846	21847 – 22427	22428 – 23170	23171 – 65536
Sample B	1 – 20531	local Otsu	local Otsu	30200 – 65536

Table 1: Global ranges of grayscale values (in 16-bit format) used for segmentation. For Sample B, a local version of the Otsu threshold is used to distinguish between binder-additive phase and polymer.

Visual comparison of grayscale images with their segmentations shows that global thresholding leads to good results for Sample A, see Figure 3. However, for Sample B, only the pore phase and the aluminum foil can be appropriately determined by global thresholding. In order to classify the remaining voxels, a local version of the Otsu threshold is used [33]. This means that for each single voxel, a cubic neighborhood with an edge length of 21 voxel units ( $= 9.24 \mu m$ ) is considered to determine Otsu’s threshold. Each of the remaining, uncategorized voxels belongs to the polymer, provided that its grayscale value is larger than the corresponding local threshold. Otherwise it is classified as part of the binder-additive phase. Finally, some post-processing steps are required. First, note that a layer of one voxel thickness around the aluminum foil is always assigned to the binder-additive phase. To remove this unrealistically segmented layer, the foil is dilated by one voxel. Second, components which are not classified as pores, but are still not connected to the aluminum foil or the electrode are removed. Moreover, connected components which

contain less than four voxels are considered as segmentation artifacts and are also removed. Examples of 2D slices of the segmented image data after post-processing are shown in Figure 3. Note that, whenever global thresholds are determined in the present study, they are determined interactively based on visual inspection, where we use the open-source software Fiji [34]. We provide 2D slices of grayscale images with the boundaries of the active material and mesopores as supplementary material. These visualizations show that the segmentation appropriately separates the different phases in Samples A and B.

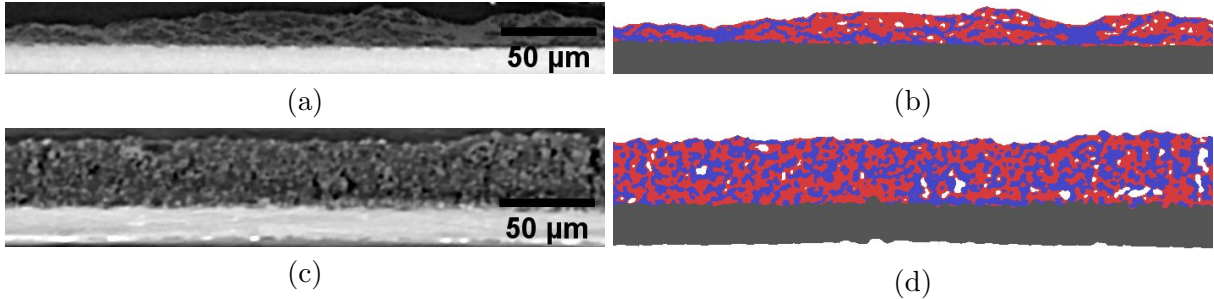


Figure 3: 2D slices of the aligned grayscale images of Sample A (top left) and Sample B (bottom left). The corresponding segmented images (after post-processing) are shown for Sample A (top right) and Sample B (bottom right). The colors blue, red, gray, and white represent the polymer phase, the binder-additive phase, the aluminum foil, and the micropores, respectively.

### 3. Results and discussion

The segmentation of 3D image data performed in Section 2.4 enables for a microstructure characterization by means of statistical image analysis. In particular, the usage of tools from spatial statistics [13, 35] reveals quantitative differences between the considered electrode materials in terms of microstructure descriptors, which are experimentally not accessible. In Section 3.1, these differences are investigated based on globally aggregated microstructure descriptors, while the variability and interdependence of local microstructure descriptors are considered in Section 3.2. The latter give insight to the heterogeneity of the electrode samples. Note that for this purpose, we only take the central and less deformed parts of the complete image data into account in order to avoid edge effects arising from bending at the boundary of the considered electrodes.

Before a quantitative microstructure characterization is performed, morphological differences between Samples A and B can be assessed by visual inspection, see Figure 4. First, Sample A is thinner compared to Sample B. Second, the polymer phase in Sample A forms large clusters, while in contrast to that, the spatial distribution of the polymer phase in Sample B is more homogeneous. Recall that the main difference in the preparation of the two electrodes is the usage of two different binders, the organo-soluble PVDF for Sample A and the water-soluble CMC for Sample B. Consequently, the slurries for electrode fabrication are processed by means of different solvents, using NMP for Sample A and water for Sample B. For Sample A, the usage of the organic solvent causes a stronger swelling of the active material PTMA (which is crosslinked). This effect leads to the larger domain sizes of the polymer phase, which can be observed in Figure 4. Third, the electrode material in Sample B seems to be less robust from a mechanical point of view, since cracks propagating through the electrode material are visible. Even if – in contrary to sample A – there is a slight bending downwards of Sample B leading to a certain tensile state, see Figure 10, we strongly assume that occurrence of cracks can be attributed to the different preparation procedures. The reason for this is that the above discussed swelling in the organic solvent

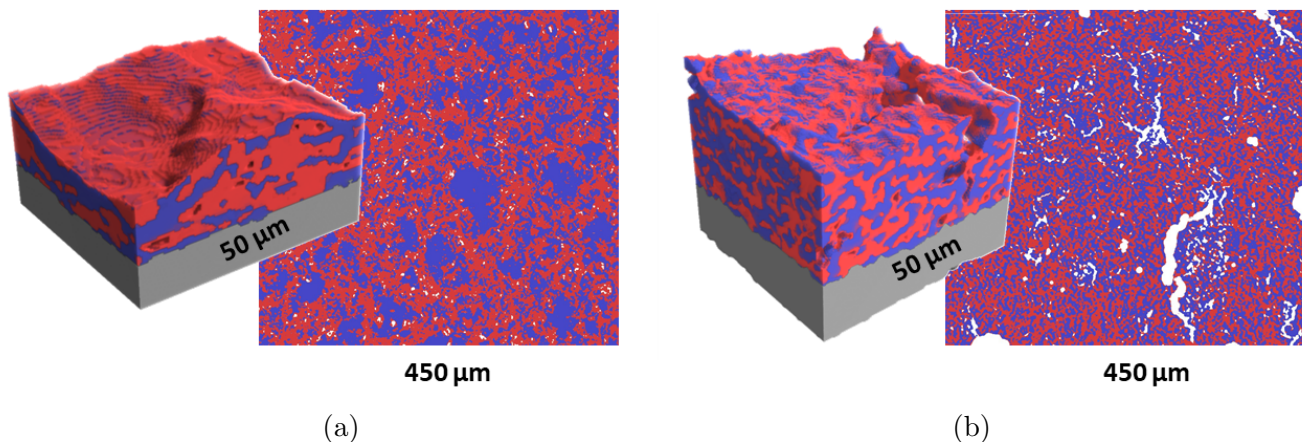


Figure 4: 3D visualization and 2D slices parallel to the aluminum foil of Sample A (left) and Sample B (right). The colors blue, red, gray, and white represent the polymer phase, the binder-additive phase, the aluminum foil, and the micropores, respectively.

of Sample A leads to a much stronger connection/adhesion between the different material domains. In contrast, PTMA is not water-soluble and therefore does not swell in the water utilized for the preparation of Sample B. Consequently, the adhesion between the different polymer particles is less pronounced leading to the formation of cracks. Note that, despite the same weight fractions of the active material and binder-additive, significant structural differences occur, which is also confirmed by the following quantitative microstructure characterization. One reason consists of the different nature of the applied binder materials and solvents used for Sample A and Sample B as well as the differences in the manufacturing process as detailed in Section 2.1. A further reason is that the following quantitative results refer to 3D image data, where the nanopores within the binder-additive phase cannot be resolved. Thus, one has to keep in mind that different nanoporosities of the utilized binder materials also influence these results.

### 3.1. Global microstructure descriptors

Besides visual comparison of Samples A and B, globally aggregated microstructure descriptors like the volume fractions of polymer, binder-additive phase, and micropores, as well as the surface area per unit volume, and various chord length distributions of the polymer phase are computed. The results obtained for the volume fractions of the three phases mentioned above are shown in Figure 5a for both samples. It turns out that Sample B exhibits a larger fraction of micropores and less binder-additive phase compared to Sample A. This coincides with the observation of cracks in Sample B which form a non-negligible part of those micropores. As detailed above, the crack formation and also the larger ratio of micropores correlates with the missing swelling of the active material in the solvent utilized for the processing of electrodes. It is important to note that these results refer to the micropores within the electrode and not to the complete pore space present within the materials. For instance, the utilized carbon material SuperP also contains nanopores; however, these can not be resolved by means of synchrotron X-ray microtomography. Due to the presence of non-resolved nanopores, the ratio of volume fractions of the polymer and binder-additive phase obtained from 3D image data (see Figure 7a) does not perfectly match the ratio of volume fractions which are obtained based on the weight fractions of active and binder-additive material as described in Section 2.1. This indicates that the formation of pores during the manufacturing process strongly influences the morphology of the considered cathodes.

In contrast to the differences observed with respect to volume fractions, the surface area per unit volume of the polymer phase is nearly identical for both samples. Note that for the computation of this quantity from discretized image data, we used the method described in [36], where we obtained the values of  $0.458 \mu\text{m}^{-1}$  for Sample A and  $0.456 \mu\text{m}^{-1}$  for Sample B. This indicates that the global surface area of polymer is not influenced by choosing different materials for the binder-additive phase during the manufacturing process. However, we will see in Section 3.2 that differences between Samples A and B can be observed with respect to the local behavior of surface area per unit volume.

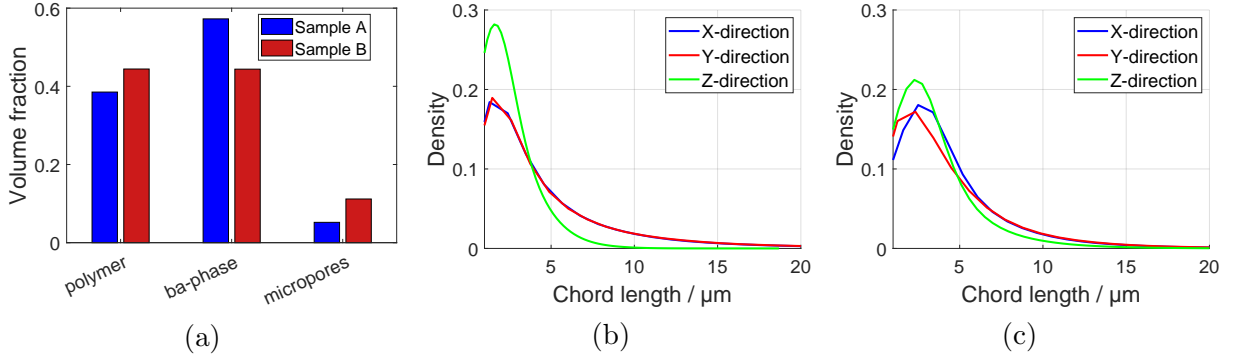


Figure 5: Global volume fractions of polymer, binder-additive-phase as well as pores of both samples are represented as a bar plot (left). The chord length distributions of the polymer phase reveal clear differences between Sample A (middle) and Sample B (right).

Furthermore, the agglomeration of the polymer phase observed in Sample A (but not in Sample B) is quantified by means of chord-length distributions of the polymer phase. Note that the chord length distribution for a predefined direction  $v$  is defined as distribution of the lengths of subsequent intersections of a randomly chosen line in direction  $v$  with the considered phase [35]. In the present contribution, the chord length distribution of polymer is computed for the three main axis directions, referred to as  $x$ -,  $y$ - and  $z$ -direction. Note that the  $xy$ -plane is parallel and the  $z$ -direction is orthogonal to the aluminum foil. The corresponding results, shown in Figures 5b and 5c, indicate –as expected considering the manufacturing process of the electrodes described in Section 2.1–that the differences of chord length distributions in  $x$ - and  $y$ -direction are negligible for both samples. However, for Sample A, chord lengths in  $x$ - and  $y$ -direction are much larger compared to those in  $z$ -direction. This coincides with the agglomeration of the polymer phase, which is only visible in the  $xy$ -plane, see Figure 3. In Sample B, such an agglomeration does not occur and, accordingly, no clear differences between the chord length distributions in  $xy$ -plane and  $z$ -direction can be observed in this case. However, in Sample B, the chord length distributions of all three main directions slightly differ from each other. This means that differences are also observed when comparing  $x$ - and  $y$ -directions. The reason for that might be the cracks which lead to local anisotropy in the microstructure.

### 3.2. Local microstructure descriptors

In order to quantify local heterogeneities of the 3D microstructure of the cathode materials considered in this contribution, we proceed similarly as in [37, 38] and, additionally, determine various local microstructure descriptors. The latter are computed for non-overlapping cutouts of the 3D image data. Thus, for both samples, we consider a square grid in  $xy$ -plane, where neighboring grid points have a distance of  $50 \mu\text{m}$  (113 voxel) from each other. Each grid point is then the center of a cutout serving as sampling window for the computation of local microstructure descriptors. The cutouts are squares in the  $xy$ -plane

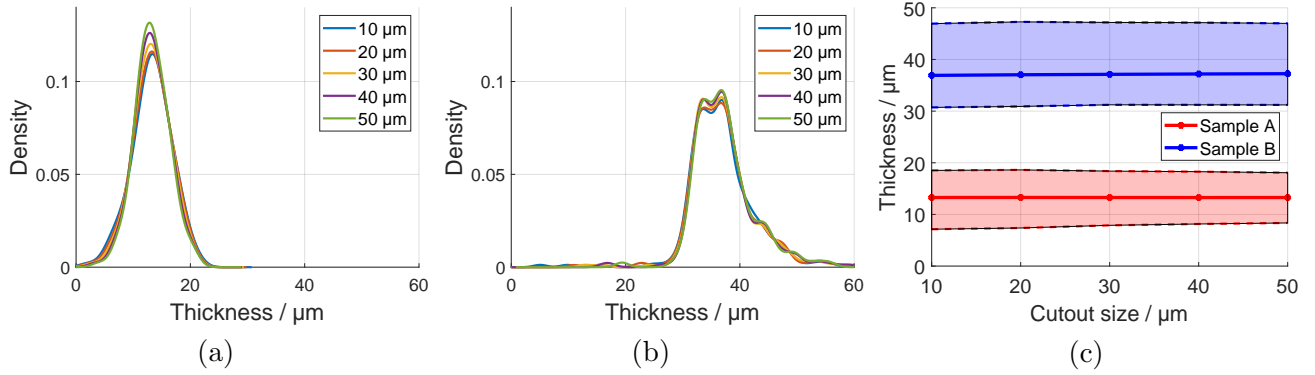


Figure 6: Distribution of local thickness for Sample A (left) and Sample B (middle). The mean value as well as the 5%- and 95%-quantiles of these distributions are shown in dependence on the considered cutout size (right).

and encompass the entire (local) extend of the sample in  $z$ -direction, where the side length of the square-shaped cutouts in the  $xy$ -plane is varied between 10  $\mu\text{m}$  (23 voxel), 20  $\mu\text{m}$  (45 voxel),  $\dots$ , 50  $\mu\text{m}$  (113 voxel). Then, for each of these cutouts their mean thickness, as well as the volume fraction and mean geodesic tortuosity of the polymer phase and binder-additive-pore phase (briefly called bap-phase) are computed, where the mean geodesic tortuosity is a measure for the lengths of shortest transportation paths within the considered phase. Furthermore, note that the bap-phase is the union of the binder-additive phase with the pore space or, in other words, the complement of the polymer phase. As a result, we obtain samples and, in this way, empirical distributions of local microstructure descriptors for each cutout size.

The distributions of local thickness are shown in Figures 6a and 6b. It can be seen that Sample B is approximately 20  $\mu\text{m}$  thicker compared to Sample A and, more interestingly, that for both samples, there is a strong variability of local thickness. The local thicknesses of Sample A vary by more than 15  $\mu\text{m}$ . There are some regions with a local thickness of less than 5  $\mu\text{m}$ , while others are more than 20  $\mu\text{m}$  thick. This variability of local thickness is even more pronounced in Sample B, where we observe a right-skewed distribution. More precisely, there is a significant amount of regions, where the cathode is 5  $\mu\text{m}$  to 10  $\mu\text{m}$  thicker than the mean of local thickness, see Figure 6c.

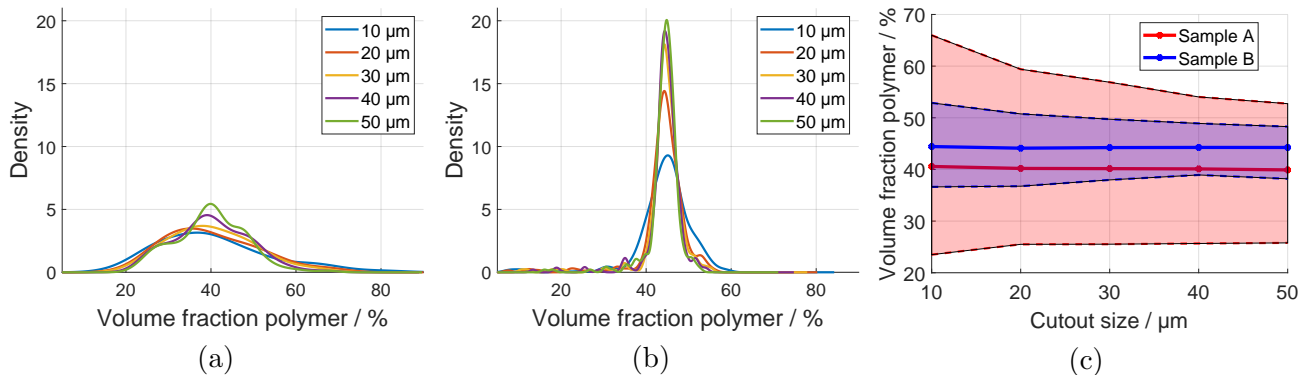


Figure 7: Distribution of local volume fractions of the polymer phase for Sample A (left) and Sample B (middle). The mean value as well as the 5%- and 95%-quantiles of these distributions are shown in dependence on the considered cutout size (right).

In Figures 7a and 7b, the distributions of local volume fractions of the polymer phase in Samples A and

B are shown for all cutout sizes. As expected, the variance decreases from smaller to larger cutouts, but further differences between these distributions for Samples A and B become clearly visible. First, while the volume fractions of the polymer phase in Sample B are concentrated between 40% and 50%, Sample A exhibits a larger variability, with values mostly between 20% and 60%. This observation is related to the thickness of the cathodes. Sample A is much thinner than Sample B (see Figure 6) and thus the averaging effect in  $z$ -direction (orthogonal to the aluminum foil) is stronger in Sample B. This explains the lower variability of local volume fractions in Sample B. Second, in contrast to Sample B, the distributions of local volume fractions of the polymer phase in Sample A are right-skewed, *i.e.*, more outliers towards large volume fractions are observed. This effect is more pronounced for small cutout sizes, which is in good accordance with the formation of polymer agglomerations quantified by the chord length distributions in Section 3.1. If a cutout intersects such an agglomeration of the polymer phase, the corresponding local volume fraction increases, where the influence is stronger for small cutout sizes. Figure 7c shows the mean values, 5% and 95%-quantiles of the distributions displayed in Figures 7a and 7b. Here one can observe that the mean volume fraction does not change when passing to larger cutout sizes, while the interval in which 90% of local volume fractions of the polymer phase are located becomes smaller with increasing cutout size.

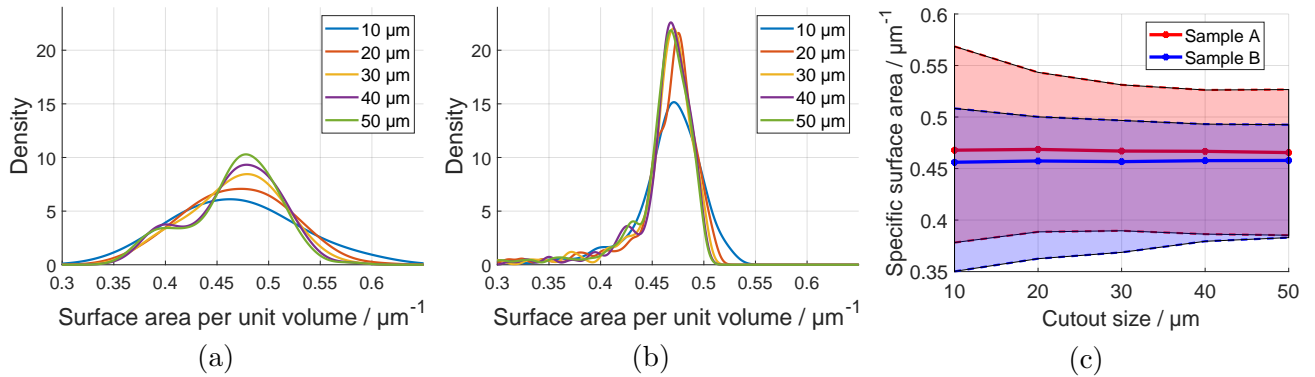


Figure 8: Distribution of local surface area per unit volume of the polymer phase for Sample A (left) and Sample B (middle). The mean value as well as the 5%- and 95%-quantiles of these distributions are shown in dependence on the considered cutout size (right).

The surface area of active material is a further important microstructure descriptor of battery electrodes, since it plays a major role for the charge transfer in an electrode. Thus, in addition to the computation of the global surface area per unit volume in Section 3.1, we also consider the local surface area per unit volume of the polymer phase. The results are presented in Figure 8. Even if the global values of the surface area per unit volume are nearly identical for both samples (see Section 3.1), we observe clearly visible differences between both samples when considering the surface area per unit volume as a local characteristic. The distribution of this quantity for Sample A has a larger variance compared to Sample B. This goes in line with the stronger variability of local volume fractions of the polymer phase in Sample A.

Finally, a microstructure descriptor quantifying the lengths of shortest transportation paths through a material's phase is considered, namely the local mean geodesic tortuosity. For this purpose, we consider transportation paths through the polymer phase and the bap-phase, respectively. For a given cutout, the corresponding local mean geodesic tortuosity is defined as the mean length of shortest transportation paths starting from the aluminum foil intersected with this cutout and going to the opposite boundary of

the cathode through the considered material phase. Note that these paths are allowed to leave the cutout serving as sampling window. For a mathematically rigorous definition of mean geodesic tortuosity, we refer to [39]. If the local mean geodesic tortuosity is close to one, most paths in the corresponding cutout go nearly straight through the transport phase. The larger this value the more tortuous those paths are.

The results of our analysis regarding local mean geodesic tortuosity are shown in Figure 9. The shortest path lengths in the polymer phase of Sample B tend to be a bit larger and their distribution is slightly skewed to the right, compared to those of the bap-phase. A reason for this might be the cracks observed in Sample B, see Figure 4b. For Sample A, however, there is a more pronounced difference between polymer and bap-phase. The local mean geodesic tortuosities of the polymer phase of Sample A are on average smaller than those of Sample B. This is reasonable, considering the larger polymer clusters in Sample A. On the other hand, the local mean geodesic tortuosities of the bap-phase of Sample A are on average considerably larger and exhibit a strong variability compared to Sample B. This is due to the fact that those paths have to circumvent large agglomerations of the polymer phase in Sample A. Because of that, some paths are up to three times longer than the thickness of the sample. Moreover, considering the mean values of local mean geodesic tortuosity of the polymer phase, we observe a critical point when increasing the cutout size from 20 to 30  $\mu\text{m}$ . For a cutout size of 20  $\mu\text{m}$  the mean value for Sample A is still between the 5%- and 95%-quantiles of Sample B, while this is not the case for cutout sizes greater or equal than 20  $\mu\text{m}$ . In other words, cutouts with a size larger than 30  $\mu\text{m}$  allow us to reliably distinguish between both samples in terms of local mean geodesic tortuosity of the polymer phase.

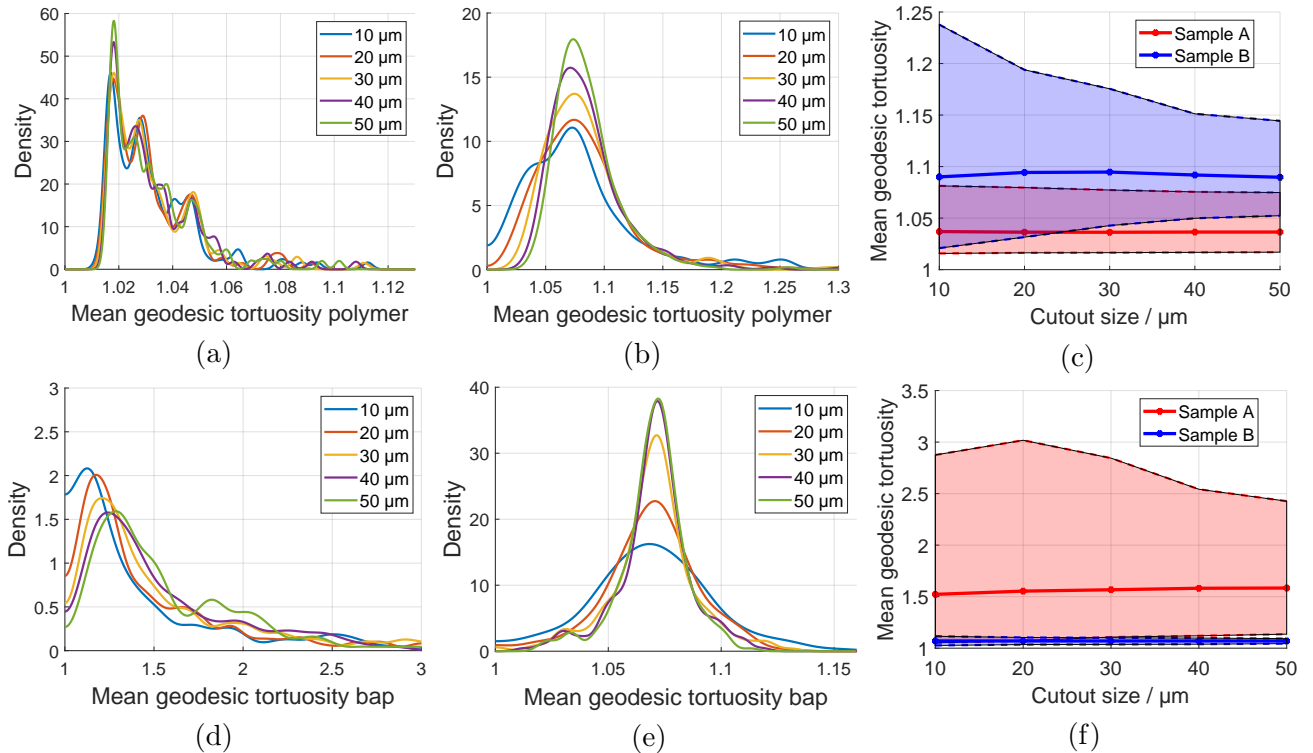


Figure 9: Distribution of local mean geodesic tortuosity of both, polymer and bap-phase for Sample A (Subfigures 4a and 4d) and Sample B (Subfigures 4b and 4e). The mean value as well as the 5%- and 95%-quantiles of these distributions are shown in dependence on the considered cutout size for the polymer (Subfigure 4c) and bap-phase (Subfigure 4e). Note that different scales are used for the plots due to the pronounced difference between Samples A and B.

### 3.3. Bivariate distributions of microstructure descriptors

So far, we have considered single local microstructure descriptors and their (univariate) probability distributions to investigate the heterogeneity of the cathode materials. Going beyond univariate distributions, we can quantify the interdependence between pairs of local microstructure characteristics by means of bivariate distributions. In Figure 10, for each of the microstructure descriptors considered in Section 3.2, the (joint) bivariate distribution as well as the corresponding 25%-, 50%-, 75%-quantiles<sup>2</sup>, of this descriptor and the local volume fraction of the polymer phase are shown.

It turns out that the bivariate distributions computed for Sample B do not seem to indicate any significant correlation between the local volume fraction of the polymer phase and any of the other previously discussed local descriptors. Interestingly, even between local volume fraction and local mean geodesic tortuosity of the polymer phase (denoted by  $\tau_{\text{polymer}}$  in Figure 10), there is, at most, only a slight correlation. A reason for this might be the fact that for Sample B the range of observed local volume fractions of the polymer phase between 40% and 50% is too small to indicate correlations. In general, higher polymer volume fractions, which lead to an increase of the number of possible pathways through the polymer, would cause a decrease of mean geodesic tortuosity. However, the additional paths, which could be created by increasing the volume fractions within the range of observed volume fractions, *e.g.* from 40% to 45%, would lead only to a slight decrease of local mean geodesic tortuosity. For Sample A, however, the local volume fraction of the polymer phase strongly influences the other local microstructure descriptors. First, we observe that for local volume fractions of polymer below 60%, this volume fraction is positively correlated with the local surface area per unit volume. For volume fractions greater than 60%, the correlation becomes negative. Even if the latter observation has to be treated carefully, since there are only a few cutouts with volume fractions greater than 60%, a negative correlation for high volume fraction is reasonable. Interestingly, for the Boolean model of stochastic geometry [13, 14, 41], which is a classical tool for mathematical modeling the microstructure of two-phase materials, the surface area per unit volume takes its maximum in the same range of volume fractions, *i.e.*, at 63%.<sup>3</sup> Note that it is well known that the performance of the electrodes is getting worse if the polymer content is too high [42]. In this case, the limitation of conduction processes in the bap-phase is too strong. Moreover, coming along with a decrease of surface area, this leads to the unfavorable effect that not the complete active material in the composite can be charged/discharged due to isolating polymer layers on the conductive additive. In this sense, the morphology of Sample B is preferable compared to Sample A, since there are less regions with a high local volume fraction of the polymer phase in Sample B.

Furthermore, a positive correlation between the local volume fraction of the polymer phase and the local mean geodesic tortuosity in the bap-phase (denoted by  $\tau_{\text{bap-phase}}$  in Figure 10) is observed. A larger amount of polymer reduces the number of possible pathways in the bap-phase, thereby increasing the length of the shortest transportation paths through the bap-phase. This strong influence of the volume fraction of the polymer phase on the mean geodesic tortuosity (also present for volume fractions between 40% and 50%) in Sample A reveals significant morphological differences compared to Sample B. The

---

<sup>2</sup>Note that there is no unique definition for quantiles of bivariate distributions [40]. In our case, the  $q$ -quantiles of the considered bivariate distributions are determined based on the estimated probability density functions as follows. We define the  $q$ -quantile  $Q_q$  of a bivariate probability density function  $f$  by  $Q_q = \{u \in \mathbb{R}^2 : f(u) = t_q\}$ , where

$$t_q = \sup \left\{ s \geq 0 : \int_{\{u \in \mathbb{R}^2 : f(u) \geq s\}} f(x) dx \geq q \right\}.$$

<sup>3</sup>This result is obtained by Mile's formulas given in Equations (3.45) and (3.46) of [13]. Furthermore, the maximum of surface area per unit volume does not depend on the choice of the distribution of grains in the Boolean model.

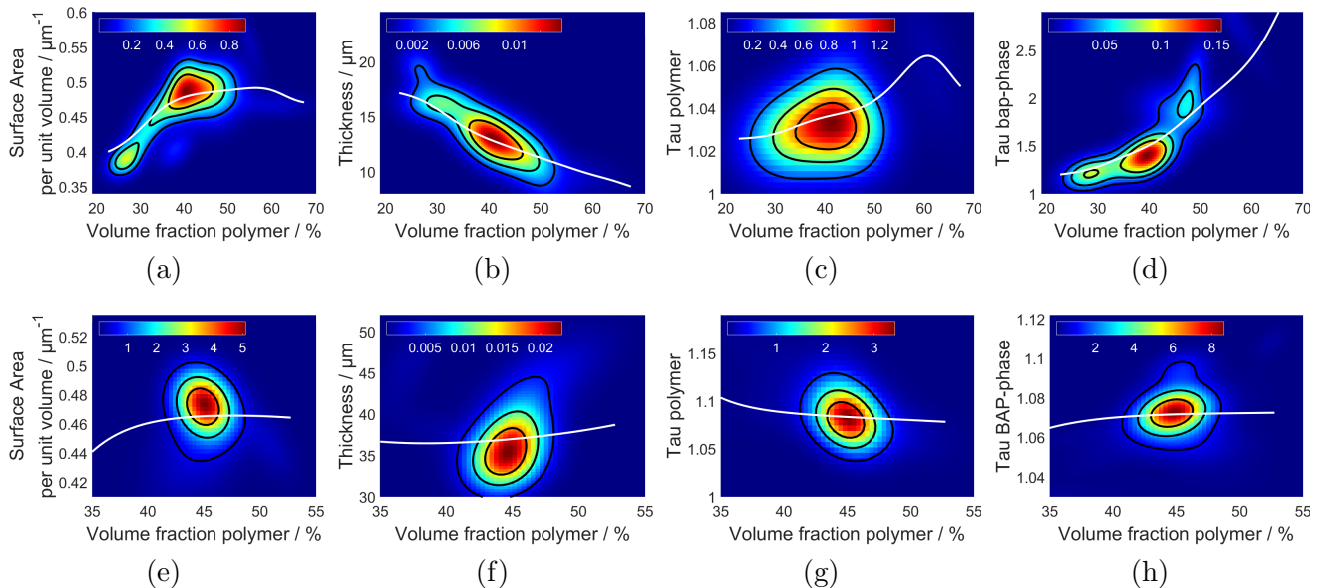


Figure 10: Bivariate distributions of pairs of local microstructure descriptors of Sample A (top row) and Sample B (bottom row) computed from cutouts with a size of  $50\ \mu\text{m}$ . The bivariate probability density functions are visualized as heat maps, where the white lines represent the (conditional) mean value for a given local volume fraction of the polymer phase. The black contour lines are the 25%-, 50%- and 75%-quantiles, respectively.

results shown in Figure 10h let us suppose that in Sample B a higher local polymer volume fraction implicates additional small polymer clusters, which have only a small effect on the length of shortest transportation paths. In Sample A however, the polymer tends to form larger, layer-like clusters, thereby blocking considerably more possible paths than the small clusters of Sample B. The local mean geodesic tortuosity of the polymer phase, on the other hand, is concentrated in a range between 1.01 and 1.05 in Sample A. This means that the morphology of the polymer phase allows for short transportation paths and—due to the minor variation of tortuosity values—we suggest not to read too much into the slightly positive (and, from a geometrical point of view, counterintuitive) correlation observed in Figure 10c. An additional result of the investigation of bivariate distributions is that, as also visible in Figure 3, the thin parts of Sample A seem to be mainly composed of polymer. This impression is supported by the results shown in Figure 10b, which indicate a negative correlation between the local volume fraction of the polymer phase and the local thickness of the cathode.

#### 4. Conclusion

For the first time, this study presents a detailed 3D microstructure characterization of polymer-based electrodes for organic radical batteries. Statistical analysis of image data gained by synchrotron X-ray tomography revealed the 3D microstructures of two polymer-based electrodes consisting of the redox-active polymer PTMA, the conductive additive SuperP and binder. The considered electrodes differ with respect to their binder materials, *i.e.*, one electrode is manufactured with PVDF and the other one with CMC. The utilization of different binder materials as well as the corresponding differences of fabrication processes led to pronounced differences of the 3D electrode microstructures. Already by visual inspection it becomes clear that manufacturing with PVDF as binder material leads to polymer clusters parallel to the aluminum foil. This electrode is more stable compared to the electrode with CMC, where—in the absence of polymer clusters—a formation of microporous cracks is observed. Moreover, statistical image

analysis allows for a quantification of these differences. While the amount of micropores in the electrode with CMC is about twice as high compared to the electrode with PVDF, the surface area per unit volume of the polymer phase is nearly identical in both electrodes. Besides a quantification of anisotropy effects in the electrode with PVDF, which are induced by the polymer clusters, local heterogeneities of the electrodes have been investigated. The results of this analysis enable us to conclude that, compared to the electrode with CMC, the electrode with PVDF is much more heterogenous and the transportation paths through the binder-additive phase are not only significantly longer on average, but local transportation paths are highly tortuous, *i.e.*, there is a non-negligible amount of paths which are twice as long as the electrode thickness. Moreover, due to the morphological differences of both electrodes, the interdependence between local volume fractions and the length of local transportation paths, is much more pronounced in the electrode with PVDF. These findings give a better understanding of the 3D microstructure of PTMA-based electrodes. They are a first step towards the optimization of polymer-based electrodes since they “bring light into the dark” and elucidate the 3D microstructure of such electrodes by a combination of experiments, 3D imaging and statistical image analysis.

### Author contributions

SM manufactured the considered electrode materials. MO, AH, and FW performed synchrotron X-ray tomography. MN and MA analyzed the image data including segmentation and statistical evaluation. MDH, USS, IM and VS conceptualized and supervised the research. All authors contributed to the interpretation of results and paper writing.

### Acknowledgements

All authors are grateful to the German Research Foundation (DFG) for funding their research projects within the framework of SPP 2248 “Polymer-based batteries” (MA 5039/7-1, SCHM 997/39-1, SCHU 1229/54-1). Furthermore, this study contributes to the research performed at CELEST (Center for Electrochemical Energy Storage Ulm-Karlsruhe). The work of MN was funded by the German Research Foundation (DFG) under Project ID 390874152 (POLiS Cluster of Excellence). SM, MDH and USS would like to thank the European Regional Development Fund (EFRE), the Thuringian Ministry for Economic Affairs, Science and Digital Society (TMWWdG) and the Thüringer Aufbaubank for their financial support.

### References

- [1] M. D. Hager, B. Esser, X. Feng, W. Schuhmann, P. Theato, and U. S. Schubert. Polymer-based batteries—flexible and thin energy storage systems. Advanced Materials, 32:2000587, 2020.
- [2] P. Poizot and F. Dolhem. Clean energy new deal for a sustainable world: from non-CO<sub>2</sub> generating energy sources to greener electrochemical storage devices. Energy & Environmental Science, 4:2003–2019, 2011.
- [3] S. Münch, A. Wild, C. Friebe, B. Häupler, T. Janoschka, and U. S. Schubert. Polymer-based organic batteries. Chemical Reviews, 116:9438–9484, 2016.
- [4] K. Nakahara, S. Iwasa, M. Satoh, Y. Morioka, J. Iriyama, M. Suguro, and E. Hasegawa. Rechargeable batteries with organic radical cathodes. Chemical Physics Letters, 359:351–354, 2002.

- [5] H. Nishide, I. Shigeyuki, Y.-J. Pu, T. Suga, K. Nakahara, and M. Satoh. Organic radical battery: nitroxide polymers as a cathode-active material. *Electrochimica Acta*, 50(2):827–831, 2004.
- [6] K. Nakahara, J. Iriyama, S. Iwasa, M. Suguro, M. Satoh, and E. J. Cairns. Al-laminated film packaged organic radical battery for high-power applications. *Journal of Power Sources*, 163:1110–1113, 2007.
- [7] D. Jeulin. Morphology and effective properties of multi-scale random sets: A review. *Comptes Rendus Mécanique*, 340:219 – 229, 2012.
- [8] S. Torquato. *Random Heterogeneous Materials: Microstructure and Macroscopic Properties*. Springer, New York, 2002.
- [9] K. Nakahara, J. Iriyama, S. Iwasa, M. Suguro, M. Satoh, and E. J. Cairns. Cell properties for modified PTMA cathodes of organic radical batteries. *Journal of Power Sources*, 165:398–402, 2007.
- [10] T. M. M. Heenan, C. Tan, J. Hack, D. J. L. Brett, and R. P. Shearing. Developments in X-ray tomography characterization for electrochemical devices. *Materials Today*, 31:69–85, 2019.
- [11] F. Tang, Z. Wu, C. Yang, M. Osenberg, A. Hilger, K. Dong, H. Markötter, I. Manke, F. Sun, L. Chen, and G. Cui. Synchrotron X-ray tomography for rechargeable battery research: Fundamentals, setups and applications. *Small Methods*, 5(9):2100557, 2021.
- [12] V. Wood. X-ray tomography for battery research and development. *Nature Reviews Materials*, 3(9):293–295, 2018.
- [13] S.N. Chiu, D. Stoyan, W.S. Kendall, and J. Mecke. *Stochastic Geometry and its Applications*. J. Wiley & Sons, Chichester, 3rd edition, 2013.
- [14] D. Jeulin. *Morphological Models of Random Structures*. Springer, Cham, 2021.
- [15] S. Barman, H. Rootzén, and D. Bolin. Prediction of diffusive transport through polymer films from characteristics of the pore geometry. *AIChE Journal*, 65(1):446–457, 2019.
- [16] B. Prifling, M. Röding, P. Townsend, M. Neumann, and V. Schmidt. Large-scale statistical learning for mass transport prediction in porous materials using 90,000 artificially generated microstructures. *Frontiers in Materials*, 8:786502, 2021.
- [17] F. Cadiou, T. Douillard, N. Besnard, B. Lestriez, and E. Maire. Multiscale characterization of composite electrode microstructures for high density lithium-ion batteries guided by the specificities of their electronic and ionic transport mechanisms. *Journal of The Electrochemical Society*, 167:100521, 2020.
- [18] A. Wagner, N. Bohn, H. Geßwein, M. Neumann, M. Osenberg, A. Hilger, I. Manke, V. Schmidt, and J. R. Binder. Hierarchical structuring of NMC111-cathode materials in lithium-ion batteries: An in-depth study of the influence of primary and secondary particle size effects on electrochemical performance. *ACS Applied Energy Materials*, 3:12565–12574, 2020.
- [19] D. Westhoff, T. Danner, S. Hein, R. Scurtu, L. Kremer, A. Hoffmann, A. Hilger, I. Manke, M. Wohlfahrt-Mehrens, A. Latz, and V. Schmidt. Analysis of microstructural effects in multi-layer lithium-ion battery cathodes. *Materials Characterization*, 151:166–174, 2019.

- [20] H. Xu, J. Zhu, D. P. Finegan, H. Zhao, X. Lu, W. Li, N. Hoffman, A. Bertei, P. Shearing, and M. Z. Bazant. Guiding the design of heterogeneous electrode microstructures for Li-ion batteries: Microscopic imaging, predictive modeling, and machine learning. Advanced Energy Materials, 11(19):2003908, 2021.
- [21] L. Zielke, T. Hutzenlaub, D. R. Wheeler, C.-W. Chao, I. Manke, A. Hilger, N. Paust, R. Zengerle, and S. Thiele. Three-phase multiscale modeling of a LiCoO<sub>2</sub> cathode: Combining the advantages of FIB-SEM imaging and X-Ray tomography. Advanced Energy Materials, 5(5), 2015.
- [22] S. J. Cooper, D. S. Eastwood, J. Gelb, G. Damblanc, D. J. L. Brett, R. S. Bradley, P. J. Withers, P. D. Lee, A. J. Marquis, N. P. Brandon, and P. R. Shearing. Image based modelling of microstructural heterogeneity in LiFePO<sub>4</sub> electrodes for li-ion batteries. Journal of Power Sources, 247:1033–1039, 2014.
- [23] S. Münch, P. Gerlach, R. Burges, M. Strumpf, S. Höppener, A. Wild, A. Lex-Balducci, A. Balducci, J. C. Brendel, and U. S. Schubert. Emulsion polymerizations for a sustainable preparation of efficient TEMPO-based electrodes. ChemSusChem, 14:449–455, 2021.
- [24] I. Khokhriakov, L. Lottermoser, and F. Beckmann. Integrated control system environment for high-throughput tomography. In Developments in X-Ray Tomography XI, volume 10391, pages 210–219. International Society for Optics and Photonics, 2017.
- [25] F. Wilde, M. Ogurreck, I. Greving, J. U. Hammel, F. Beckmann, A. Hipp, L. Lottermoser, I. Khokhriakov, P. Lytaev, T. Dose, H. Burmester, M. Müller, and A. Schreyer. Micro-CT at the imaging beamline P05 at PETRA III. In AIP Conference Proceedings, volume 1741, 030035, 2016.
- [26] J. Moosmann, A. Ershov, V. Weinhardt, T. Baumbach, C. LaBonne, X. Xiao, J. Kashef, and R. Hofmann. Time-lapse X-ray phase-contrast microtomography for in vivo imaging and analysis of morphogenesis. Nature Protocols, 9:294–304, 2014.
- [27] W. van Aarle, W.J. Palenstijn, J. Cant, E. Janssens, F. Bleichrodt, A. Dabravolski, J. De Beenhouwer, K.J. Batenburg, and J. Sijbers. Fast and flexible X-ray tomography using the ASTRA toolbox. Optics Express, 24(22):25129–25147, 2016.
- [28] W. Görner, M.P. Hentschel, B.R. Müller, H. Riesemeier, M. Krumrey, G. Ulm, W. Diete, U. Klein, and R. Frahm. BAMline: the first hard X-ray beamline at BESSY II. Nuclear Instruments and Methods in Physics Research Section A: Accelerators, Spectrometers, Detectors and Associated Equipment, 467–468:703–706, 2001.
- [29] D. Gürsoy, F. De Carlo, X. Xiao, and C. Jacobsen. TomoPy: A framework for the analysis of synchrotron tomographic data. In S. R. Stock, editor, Developments in X-ray Tomography IX, volume 9212, pages 162–165. International Society for Optics and Photonics, 2014.
- [30] L.I. Rudin, S. Osher, and E. Fatemi. Nonlinear total variation based noise removal algorithms. Physica D: Nonlinear Phenomena, 60(1):259–268, 1992.
- [31] A. Buades, B. Coll, and J.-M. Morel. A non-local algorithm for image denoising. In Proceedings of the 2005 IEEE Computer Society Conference on Computer Vision and Pattern Recognition, volume 2, pages 60–65, USA, 2005. IEEE Computer Society.
- [32] P. Soille. Morphological Image Analysis: Principles and Applications. Springer, New York, 2003.

- [33] N. Otsu. A threshold selection method from gray-level histograms. IEEE Transactions on Systems, Man, and Cybernetics, 9(1):62–66, 1979.
- [34] J. Schindelin, I. Arganda-Carreras, E. Frise, V. Kaynig, M. Longair, T. Pietzsch, S. Preibisch, C. Rueden, S. Saalfeld, B. Schmid, J.-Y. Tinevez, D. W. White, V. Hartenstein, K. Eliceiri, P. Tomancak, and A. Cardona. Fiji: an open-source platform for biological-image analysis. Nature Methods, 9(7):676, 2012.
- [35] J. Ohser and K. Schladitz. 3D Images of Materials Structures: Processing and Analysis. J. Wiley & Sons, Weinheim, 2009.
- [36] K. Schladitz, J. Ohser, and W. Nagel. Measuring intrinsic volumes in digital 3D images. In A. Kuba, L. Nyúl, and K. Palágyi, editors, 13th International Conference Discrete Geometry for Computer Imagery, pages 247–258. Springer, Berlin, 2007.
- [37] M. Neumann, E. Machado-Charry, E. Baikova, A. Hilger, U. Hirn, R. Schennach, I. Manke, V. Schmidt, and K. Zojer. Capturing centimeter-scale local variations in paper pore space via  $\mu$ -CT: A benchmark study using calendered paper. Microscopy and Microanalysis, 27:1305–1315, 2021.
- [38] M. Neumann, E. Machado-Charry, K. Zojer, and V. Schmidt. On variability and interdependence of local porosity and local tortuosity in porous materials: a case study for sack paper. Methodology and Computing in Applied Probability, 23:613–627, 2021.
- [39] M. Neumann, C. Hirsch, J. Staněk, V. Beneš, and V. Schmidt. Estimation of geodesic tortuosity and constrictivity in stationary random closed sets. Scandinavian Journal of Statistics, 46:848–884, 2019.
- [40] R. Serfling. Quantile functions for multivariate analysis: approaches and applications. Statistica Neerlandica, 56:214–232, 2002.
- [41] I. Molchanov. Statistics of the Boolean Model for Practitioners and Mathematicians. J. Wiley & Sons, Chichester, 1997.
- [42] J.-K. Kim, G. Cheruvally, J.-H. Ahn, Y.-G. Seo, D. S. Choi, S.-H. Lee, and C. E. Song. Organic radical battery with PTMA cathode: Effect of PTMA content on electrochemical properties. Journal of Industrial and Engineering Chemistry, 14:371–376, 2008.

### Supplementary material

As an extension of Figure 3, the same 2D slices of aligned grayscale images are shown in Figures 11 and 12 for Samples A and B, respectively, where the boundary of the polymer phase as well as the boundary of the mesopores are additionally visualized. Thereby, we provide a further visual underpinning of the quality of the segmentation described in Section 2.4.

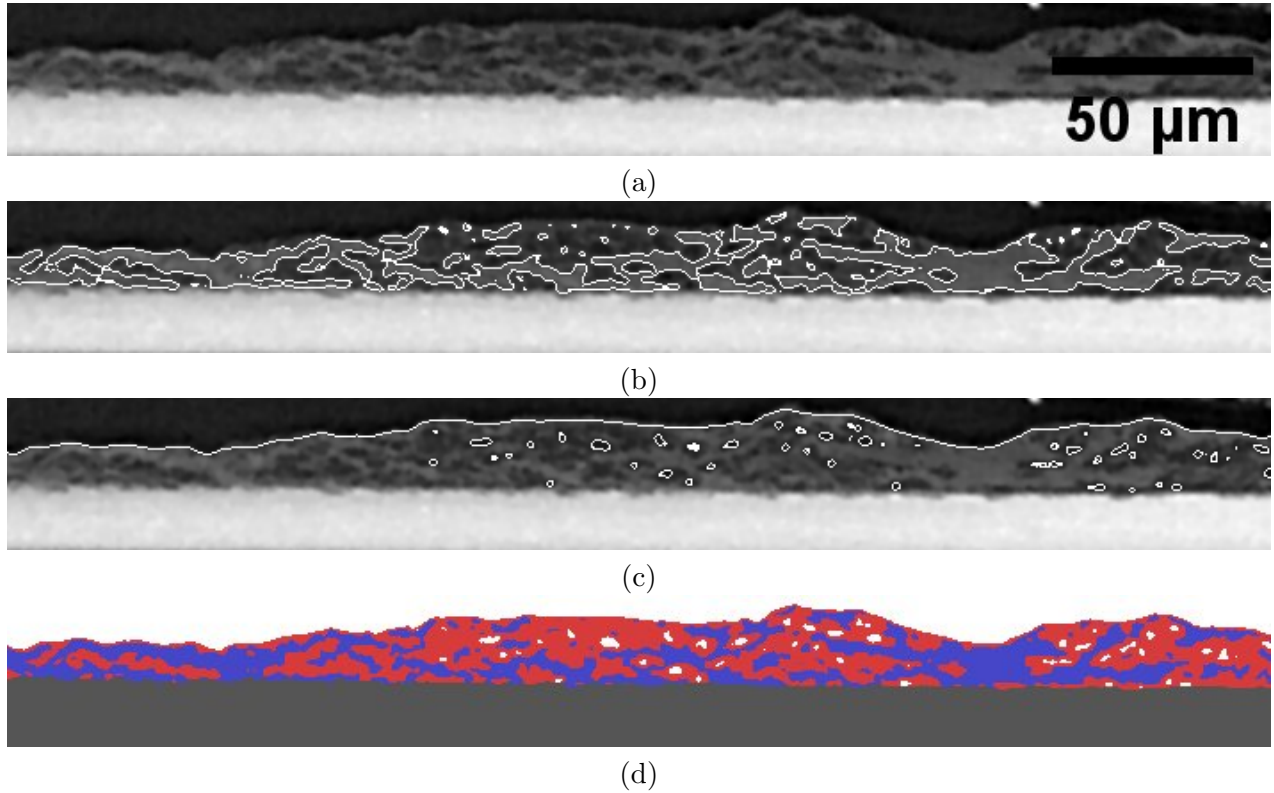


Figure 11: 2D slice of the aligned grayscale image data of Sample A highlighting the contrast differences between active material, binder-additive and pore phase. The images shown in (b) and (c) are the grayscale image from (a) with the boundaries of the active material (b) and background/mesopores (c) shown as white lines. The final segmentation is shown in (d) with blue representing the active material, red the binder-additive phase, gray the aluminum foil and white the background/mesopores.

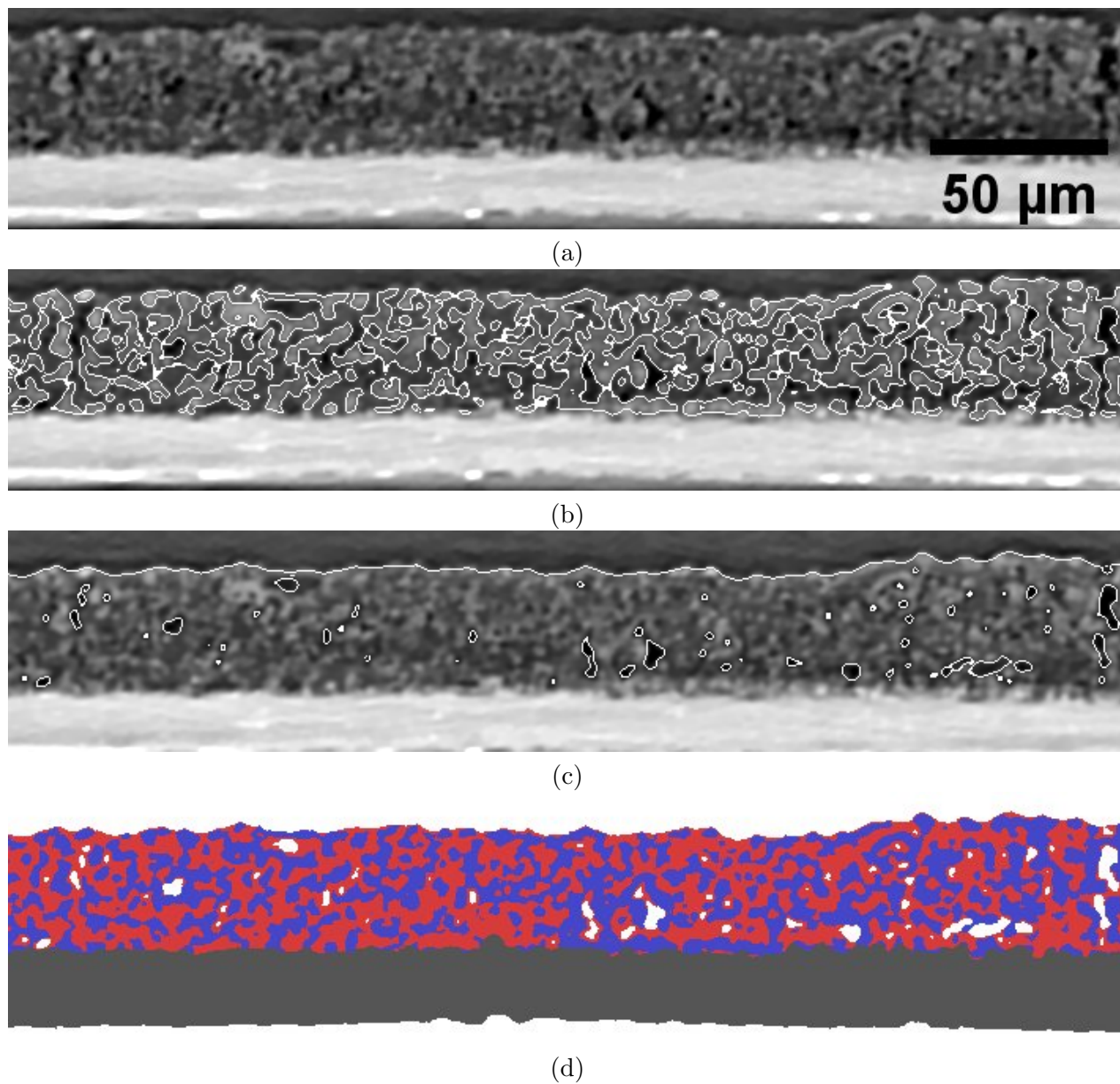


Figure 12: 2D slice of the aligned grayscale image data of Sample B highlighting the contrast differences between active material, binder-additive and pore phase. The images shown in (b) and (c) are the grayscale image from (a) with the boundaries of the active material (b) and background/mesopores (c) shown as white lines. The final segmentation is shown in (d) with blue representing the active material, red the binder-additive phase, gray the aluminum foil and white the background/mesopores.